# Energy Harvesting from the Animal/Human Body for Self-Powered Electronics

Canan Dagdeviren,[1,2] Zhou Li,[3] and Zhong Lin Wang[3,4]

[1]Media Lab, Massachusetts Institute of Technology, Cambridge, Massachusetts 02139; email: canand@mit.edu

[2]Harvard Society of Fellows, Harvard University, Cambridge, Massachusetts 02138

[3]Beijing Institute of Nanoenergy and Nanosystems, Chinese Academy of Sciences, National Center for Nanoscience and Technology, Beijing 100083, People's Republic of China

[4]School of Materials Science and Engineering, Georgia Institute of Technology, Atlanta, Georgia 30332; email: zlwang@gatech.edu

Annu. Rev. Biomed. Eng. 2017. 19:85–108

The *Annual Review of Biomedical Engineering* is online at bioeng.annualreviews.org

https://doi.org/10.1146/annurev-bioeng-071516-044517



## Keywords

energy harvesting, biofuel cell, thermoelectricity, triboelectricity, piezoelectricity, self-powered electronics, mechanically adaptive electronics

## Abstract

Living subjects (i.e., humans and animals) have abundant sources of energy in chemical, thermal, and mechanical forms. The use of these energies presents a viable way to overcome the battery capacity limitation that constrains the long-term operation of wearable/implantable devices. The intersection of novel materials and fabrication techniques offers boundless possibilities for the benefit of human health and well-being via various types of energy harvesters. This review summarizes the existing approaches that have been demonstrated to harvest energy from the bodies of living subjects for self-powered electronics. We present material choices, device layouts, and operation principles of these energy harvesters with a focus on in vivo applications. We discuss a broad range of energy harvesters placed in or on various body parts of human and animal models. We conclude with an outlook of future research in which the integration of various energy harvesters with advanced electronics can provide a new platform for the development of novel technologies for disease diagnostics, treatment, and prevention.

## Contents





## 1. INTRODUCTION

Recent advances in wearable/implantable devices have attracted significant attention from both academia and industry due to their notable applications in health monitoring, disease prevention, diagnostics, and treatment (1–3). Most of these systems, however, still use batteries as power supplies; batteries' limited capacity and large size constrain their lifetime and overall dimensions, respectively (4, 5). Using higher-capacity batteries is not ideal, because battery capacity is usually linearly dependent on battery volume. Promising alternative solutions have been developed in which energy from the ambient environment can be extracted by use of energy harvesters to generate power. Energy harvesters can provide complementary power to prolong the battery lifetime of wearable/implantable devices, or can even function as the sole power supply.

Although there are various applicable energy sources for harvesters, including sunlight, IR light from the environment, and radio-frequency power sources through inductive coupling (6), the body of a living subject is a particularly favorable energy source, given the vast number and wide variety of available energies (7, 8). For instance, theoretical calculations have demonstrated that body heat, breathing, and arm movements can generate 2.8–4.8 W, 0.83 W, and 60 W, respectively (8). Although these power sources could offer a compelling way to accommodate the operation of a cardiac pacemaker (50 μW for 7 years), a hearing aid (1 mW for 5 days), and a smartphone (1 W for 5 h) (9), practical demonstrations are needed to show the feasibility of powering such electronics.

Given the various approaches to harvesting energies from living subjects (6, 10), this review specifically addresses those based on biofuel cells (BFCs) (7, 11), thermoelectricity (12, 13), triboelectricity (14), and piezoelectricity (15–18) (**Figure 1**). This article begins with an overview of the material considerations for each of these approaches, followed by an outline of their respective operation principles. We then discuss typical energy harvester configurations based on these mechanisms in order to provide a comprehensive picture of recent progress. Finally, we conclude by briefly discussing future directions and opportunities in the energy harvesting field.

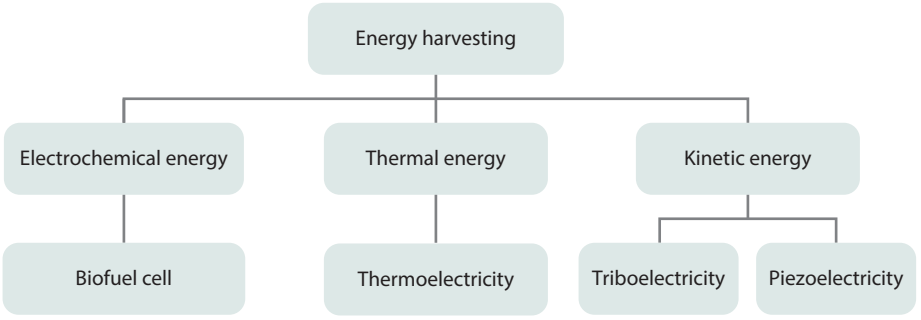


**Figure 1**

An overview of potential sources for energy harvesting from the bodies of living subjects.



## 2. MATERIAL CHOICES TO CREATE ENERGY HARVESTERS

### 2.1. Fuels and Enzymes for Biofuel Cells

Glucose is one of the primary sources of energy in the bodies of living subjects, and a BFC is ideal for extracting this type of fuel to generate electricity (19–22), as discussed in Section 3.1. Sweat lactate represents another type of fuel; it is generated outside the human body during perspiration, eliminating the need to implant a BFC within the body (23). Although glucose and sweat lactate function as fuels, enzymes serve as the catalyst for oxidation and reduction reactions. For a glucose BFC (GBFC), the most common enzymes are glucose oxidase (GOx) for the oxidization of glucose at the anode (**Figure 2*a***) and laccase for dioxygen reduction at the cathode (24). Several studies have demonstrated the feasibility of using GOx for in vivo BFCs (25, 26), but safety concerns limit the use of this enzyme. These concerns arise from the generation of hydrogen peroxide by GOx that could affect the stability of anodic and cathodic enzymes, deteriorating the system's performance, and long-term use in the body could be harmful (27).

An alternative enzyme is $NAD^+$-GDH (nicotinamide adenine dinucleotide, oxidized form–dependent glucose dehydrogenase). Use of this enzyme, however, requires the presence of $NAD^+$ coenzyme in the solution (28). Therefore, the fabrication of a robust, implantable BFC by GDH requires a selective membrane and is complicated to perform, as the BFC has to be in partial contact with body fluid (29, 30). An enzyme that can be used with GBFCs that does not suffer from these problems is PQQ-GDH (pyrroloquinoline quinone–dependent glucose dehydrogenase) (7, 31–33), which allows direct transfer of electrons to the electrode for efficient operation (34).

For sweat lactase–based fuel cells, the lactate oxidase (LOx) enzyme mediated by TTF · TCNQ (tetrathiafulvalene 7,7,8,8-tetracyanoquinodimethane) is of interest because it provides the necessary power density to operate wearable electronics, unlike other enzymes (e.g., lactate dehydrogenase enzyme and LOx) (23).

Another key design parameter of a BFC is the enzyme–electrode interface, which is constructed such that the electron transfer between the enzyme and electrodes is stable and efficient (35). In their natural form, enzymes move freely within biological cells. The operation of a BFC, however, requires the enzymes to be localized in a particular region, which can be done either physically (e.g., via gel entrapment or adsorption) or chemically (e.g., via covalent immobilization) (34, 36). The selection of electrode material is also crucial for the design of BFCs. For instance, carbon nanotubes (CNTs) are a type of electrode that has attracted a great deal of attention due to their electroactive surface (37–41). **Figure 2*b*** shows a scanning electron microscopy (SEM) image of

common CNTs that serve as the conductive support for enzyme-modified electrodes. The large surface area of CNTs enables high-density immobilization of enzymes, providing high current density to the system (41). The CNTs' electrodes also enable direct electron transfer due to their ability to access the enzymes' embedded active site. Therefore, CNTs, either randomly deposited or vertically aligned, are an excellent candidate material for a BFC electrode.

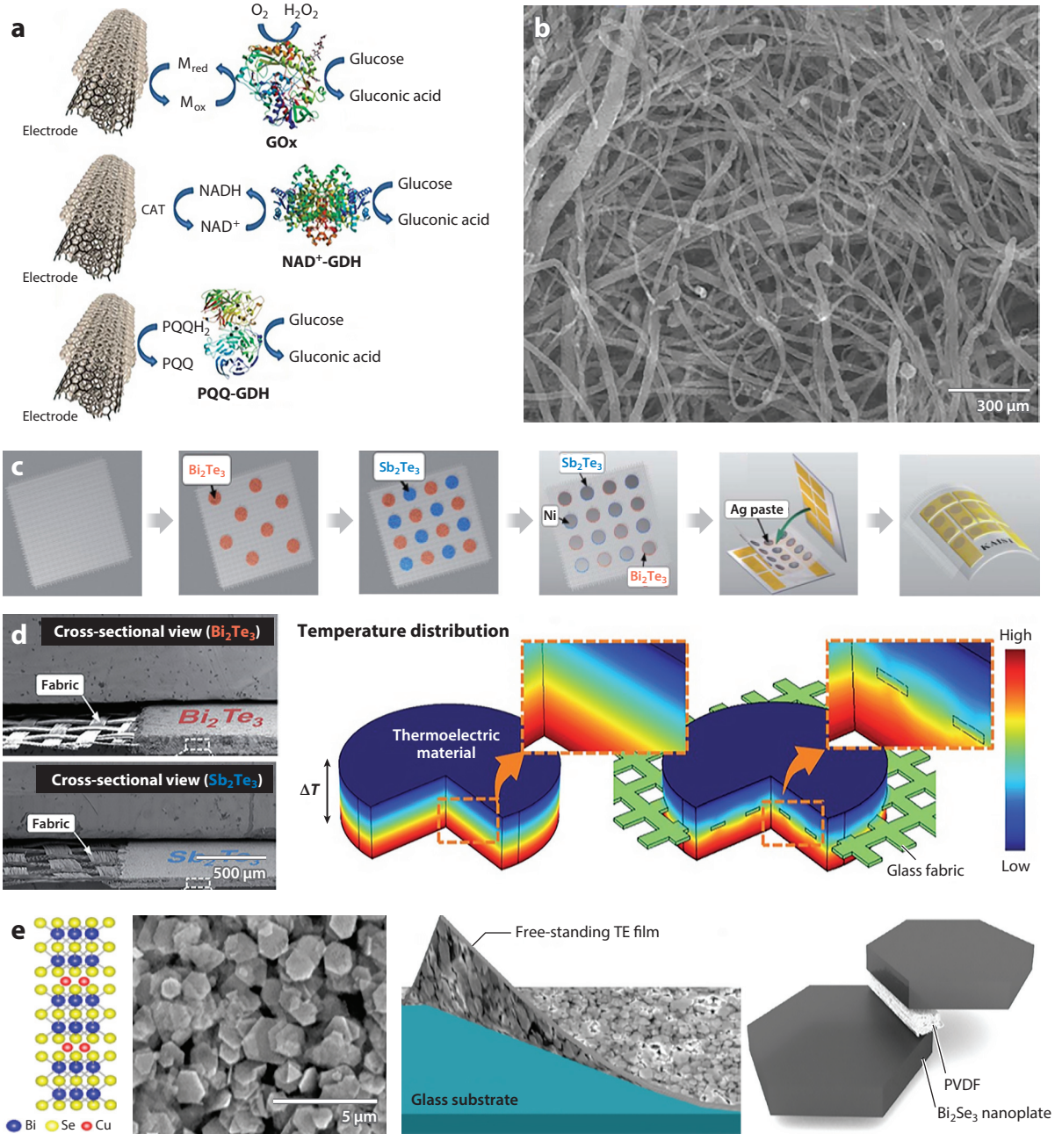

## 2.2. Thermoelectric Materials

Body heat is a natural source of energy (8) that can be harnessed via the thermoelectric effect. Extracted heat from the human body is enough to power implanted stimulators and sensors, such as deep-brain stimulators, artificial cochleas, and wireless health monitors (6, 42). Promising candidates for flexible thermoelectric generators (TEGs) for use in self-powered wearable electronics range from bulk crystallines, such as bismuth telluride ($Bi_2Te_3$) (42–45), bismuth selenide ($Bi_2Se_3$) (46), tin selenide (SnSe) (47), tin telluride (PbTe) (48, 49), and silicon germanium (SiGe) (50), to thermoelectric polymers and composites. Additionally, many studies have demonstrated that conducting polymers, such as polyaniline (51, 52), polypyrrole (53, 54), and poly(3,4-ethylenedioxythiophene)-polystyrene sulfonate (55, 56), are suitable for the fabrication of organic material–based TEGs (57, 58). Indeed, different ways to fabricate TEGs have been studied extensively (50, 59, 60). One approach uses nonplanar stepper lithography to form a large depth of focus and high–aspect ratio structures that are crucial to achieve high-performance energy harvesters (50). An alternative approach is to employ screen-printing techniques to form thin (~500-μm), flexible, inorganic thermoelectric films (59), which are laid on top of a glass fabric–based textile (**Figure 2*c*,*d***). In composite form, the integration of polyvinylidene fluoride (PVDF) with copper-doped $Bi_2Se_3$ nanoplates (**Figure 2*e***) provides flexibility as well as a high-temperature power factor and thermoelectric figure of merit, which are important for high energy-conversion efficiency (60).

## 2.3. Triboelectric Materials

Body movement is a primary source of mechanical energy (61). One way to harness this energy involves triboelectric materials. These materials utilize the triboelectrification effect, whereby a specific material becomes electrically charged following contact with a different material (14). This phenomenon exists in almost all materials, both natural and synthetic, ranging from metals to polymers. **Figure 3** summarizes a wide array of material choices for triboelectric nanogenerators (TENGs), showing their tendency to gain or lose electrons, depending on their polarity (14). Ideally, one should use two materials that are located far apart from one another in the triboelectric series in order to attain a high rate of charge transfer.

To enhance the contact area and triboelectrification, it is essential to physically modify the surface morphologies into various patterns, such as lines, cubes, wires, pyramids, squares, and porous micro/nanopatterns (**Figure 3**) (14, 62–70). Although these patterns can increase the friction force, they may also affect the TENG's conversion efficiency. The design of such surface morphologies, therefore, should be balanced with optimum conversion efficiency in order to achieve an effective system. Another way to improve surface electrification as well as the materials'

**Figure 2**

Materials for biofuel cells and thermoelectric (TE) energy harvesters. (*a*) Glucose oxidation through different enzymes associated with carbon nanotubes (CNTs) as the conductive support: glucose oxidase (GOx), nicotinamide adenine dinucleotide, oxidized form–dependent glucose dehydrogenase ($NAD^+$-GDH), and pyrroloquinoline quinone–dependent glucose dehydrogenase (PQQ-GDH) operating electron transfer to CNTs (22). (*b*) A scanning electron microscope (SEM) image of CNTs used as conductive support for enzyme-modified electrodes (22). (*c*) The fabrication process of a flexible TE generator module made of $Bi_2Te_3$ and $Sb_2Te_3$ thick films on glass fabric (59). (*d*) (*Left*) SEM images of $Bi_2Te_3$ and $Sb_2Te_3$ thick films. (*Right*) Simulation of the temperature distribution across the TE film without and with the glass fabric (59). (*e*) (*From left to right*) A schematic crystal structure of copper-intercalated $Bi_2Se_3$, SEM images of $Bi_2Se_3$ nanoplates, $Bi_2Se_3$ nanoplate/polyvinylidene fluoride (PVDF)-based *n*-type flexible TE films, and the PVDF barrier between two $Bi_2Se_3$ nanoplates (60).

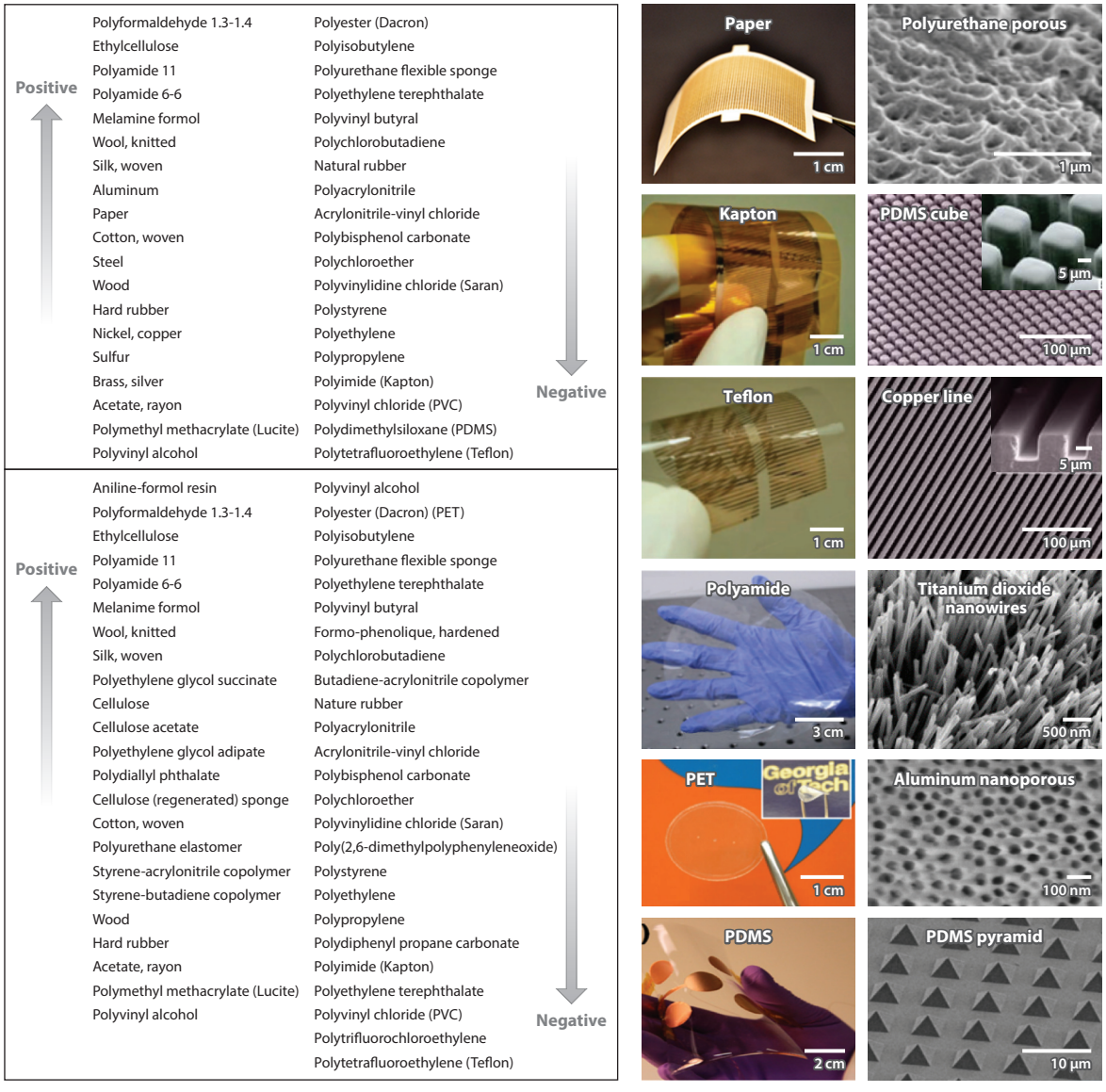


**Figure 3**

Materials for triboelectric energy harvesters. The triboelectric series for various common materials shows their tendency to easily lose electrons (positive) and gain electrons (negative) (14). These materials include metals, stable polymers, and organic and biodegradable polymers (62–70).

permittivity, which enables electrostatic induction (14), is to embed nanoparticles in a polymer matrix to form a composite contact material.

## 2.4. Piezoelectric Materials

Piezoelectric materials can also be used to harness mechanical energy from living subjects via mechanical-to-electrical transduction mechanisms. Inorganic piezoelectric materials, such as lead

zirconate titanate (PZT) and zinc oxide (ZnO), lack central symmetry in their crystal structure, causing a reconfiguration of dipole-inducing ions that enables energy conversion for power generation under external strain (71, 72). Organic piezoelectric materials, such as PVDF and PVDF-TrFE [poly(vinylidenefluoride-*co*-trifluoroethylene)] (73), are preferable because they have an inherently flexible nature that enables conformal integration to the curvilinear surfaces of the body. **Figure 4*a*** shows an example of an organic piezoelectric material, PVDF (74, 75), demonstrating its ability to conform to the aorta of a pig.

In terms of piezoelectric coefficients, inorganic materials perform better than organic materials. Because bulk inorganic materials are brittle and rigid, and thus not amenable for use on the soft surfaces of the body, several groups have fabricated them into thin films, membranes/ribbons, or nanowires (NWs) (76–78) to form more-flexible systems. These materials can also be formed into a hemisphere structure embedded in a polymer matrix, which offers not only flexibility but also stretchability that broadens the range of its applications (79). Thus, deformation of such structures permits the system to be stretched by up to 40% of strain, without any mechanical fractures (79). SEM images, bending experiments, and simulations (**Figure 4*b*,*c***) show that PZT nanofibers and thin films (15, 80, 81), as well as barium titanate ($BaTiO_3$) thin films (**Figure 4*d***) (82), are more flexible than their bulk counterparts. In addition to those structures, ZnO NWs (83–85), $(1-x)Pb(Mg_{1/3}Nb_{2/3})O_{3-x}PbTiO_3$ (PMN-PT) thin films (86), and $Ba(Zr_{0.2}Ti_{0.8})O_{3-x}(Ba_{0.7}Ca_{0.3})TiO_3$ (BZT-BCT) NW/polydimethylsiloxane (PDMS) nanocomposites (87) have been used to create flexible systems that facilitate intimate integration with various body parts. Several groups have demonstrated the capability of these systems to harness mechanical movements of limbs and natural vibrations or motions of internal organs and vessels (15–18, 74, 79, 86, 88–91).

## 3. OPERATION PRINCIPLES OF VARIOUS ENERGY HARVESTERS

### 3.1. Biofuel Cells

In general, power generation through BFCs is similar to that through commercial fuel cells, such that both involve reduction–oxidation reactions. For example, a GBFC, as described in Section 2.1, employs glucose oxidation at the anode and oxygen reduction at the cathode to generate electrical power (92–94). The cell consists of two electrodes (anode and cathode) that are separated into two different compartments and connected in the circuit through an external variable load resistance (**Figure 5*a***). The electrochemical reactions of a GBFC can be described as follows (93):

$$\text{anode: } C_6H_{12}O_6 + 2OH^- \rightarrow C_6H_{12}O_7 + H_2O + 2e^-,$$

$$\text{cathode: } \frac{1}{2}O_2 + H_2O + 2e^- \rightarrow 2OH^-,$$

$$\text{overall: } C_6H_{12}O_6 + \frac{1}{2}O_2 \rightarrow C_6H_{12}O_7,$$

$$\Delta G^0 = 0.251 \times 10^6 \text{ J/mol},$$

$$U^0 = 1.30 \text{ V},$$

where $\Delta G^0$ is the standard free energy and $U^0$ is the theoretical cell voltage. The system performance of a GBFC can be further evaluated in terms of the recorded current and voltage output values during device operation.

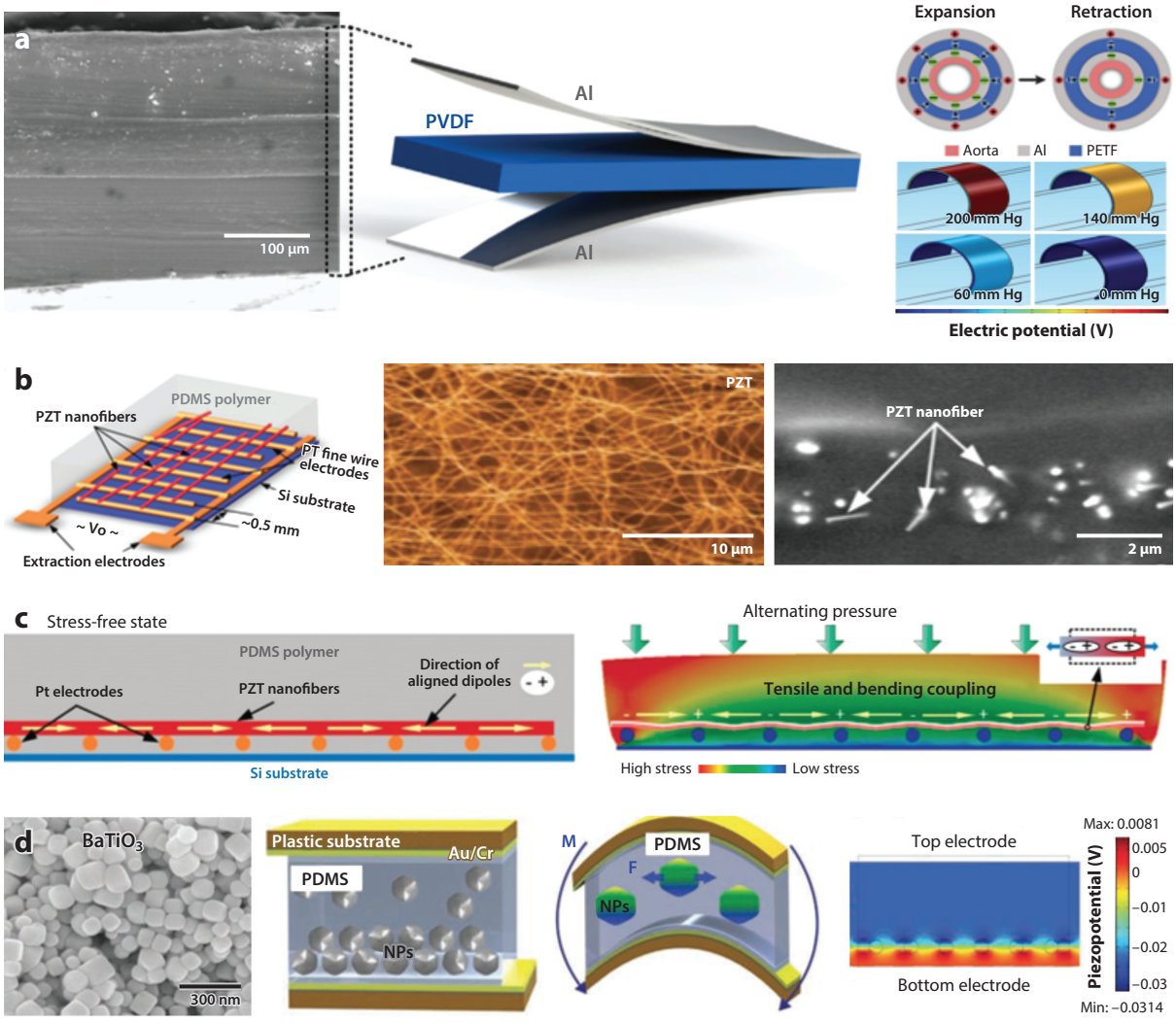


**Figure 4**

Examples of organic and inorganic piezoelectric materials. (*a*) (*From left to right*) A cross-sectional scanning electron microscope (SEM) image of a piezoelectric generator (PG), a schematic illustration of a PG, the charge distributions in the device during expansion and retraction states, and the generated electric potential under different blood pressure values (74, 75). (*b*) (*From left to right*) A schematic view of a lead zirconate titanate (PZT) nanofiber generator, a SEM image of a PZT nanofiber, and a cross-sectional SEM image of the PZT nanofibers in a polydimethylsiloxane (PDMS) matrix (80). (*c*) (*From left to right*) A cross-sectional view of the poled PZT nanofibers in the generator and a schematic view of the power output mechanism of the PZT nanofibers (80). (*d*) (*From left to right*) A SEM image of $BaTiO_3$ nanoparticles (NPs), schematics of the cross-sectional structure of a nanocomposite generator (NCG), and the calculated piezopotential distributions in the NCG (82). Abbreviation: PVDF, polyvinylidene fluoride.

## 3.2. Thermoelectric Generators

A TEG harvests body heat through direct contact with the human body and operates according to the Seebeck effect: Voltage is generated when there is a temperature gradient between the hot and cold junctions (see Section 2.2) (9). The essential mechanism of a TEG, which employs fabric and thermocouples, was described in a recent study (95). In this type of system, the output voltage is

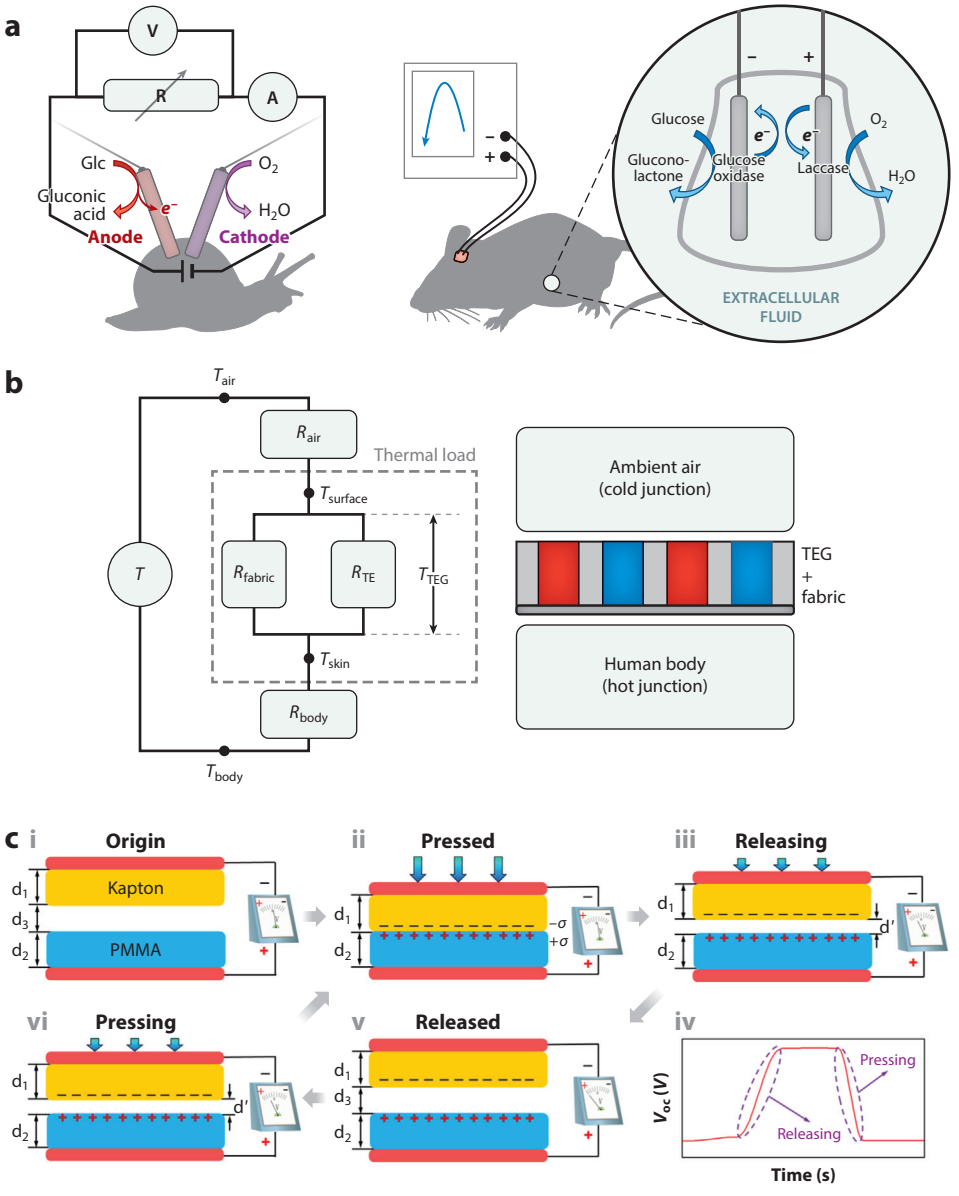


## Figure 5

Operation principles of various types of energy harvesters. (*a*) Illustrations of biofuel cell operations on (*left*) a snail (7) and (*right*) a rat (94). (*b*) (*Left*) A circuit model and (*right*) an illustration of a thermoelectric generator (TEG) for extracting body heat to generate electricity (95). (*c*,*d*) An illustration of the working mechanism of a triboelectric nanogenerator in (*c*) contact separation mode for open circuit condition (96) and (*d*) full cycle sliding operation mode (97). (*e*,*f*) Schematic diagrams of the working mechanism of a piezoelectric (*e*) nanowire (99) and (*f*) membranes/ribbons (101). Abbreviations: CB, conduction band; *e*, electron; $E_F$, Fermi energy; G, the grounded end of a nanowire; PMMA, poly(methylmethacrylate); PTFE, polytetrafluoroethylene; T, the other end of the nanowire to be pushed by a conductive atomic force microscope tip; VB, valence band; $\Phi_{SB}$, barrier height.

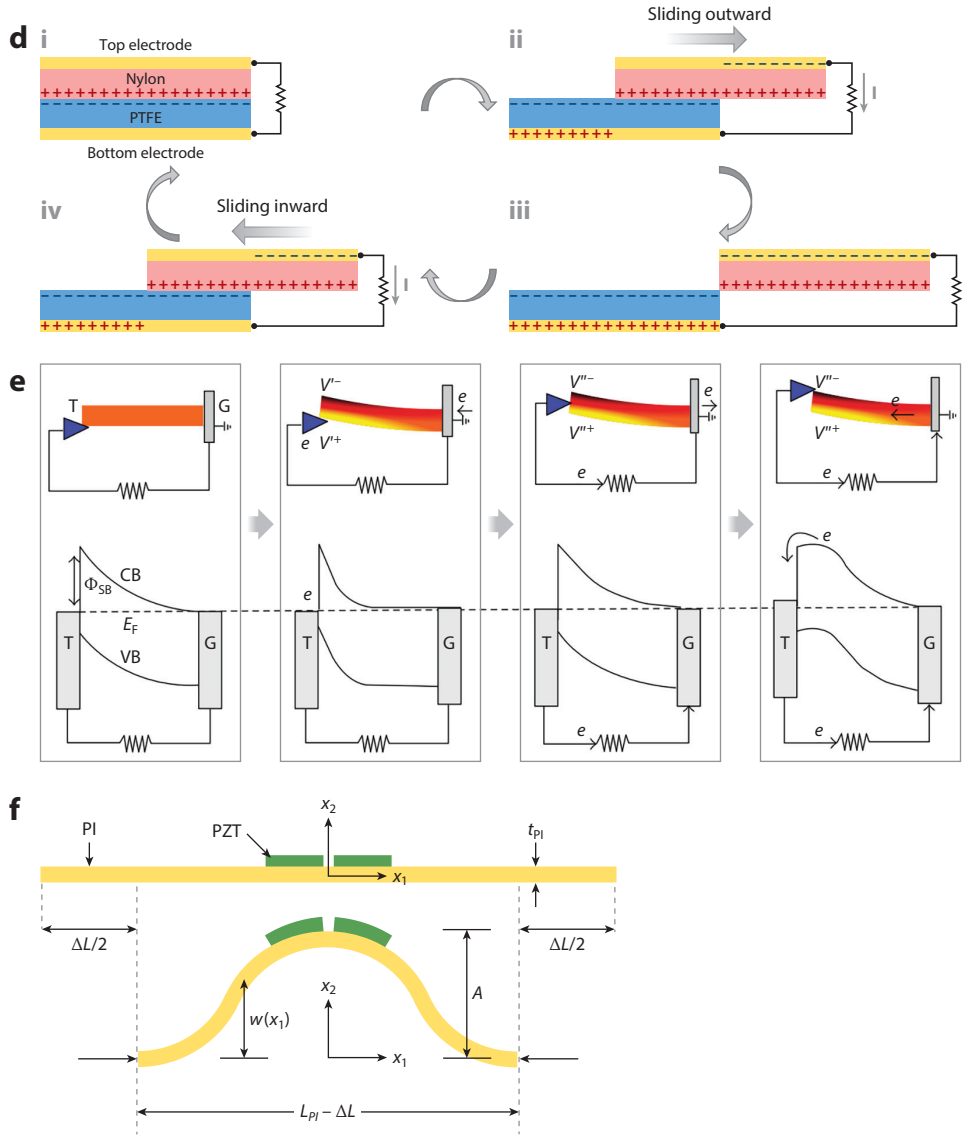


**Figure 5**

(*Continued*)

defined as $V = n\alpha\Delta T_{\mathrm{TEG}}$, where $n$ is the number of thermocouples, $\alpha$ is the Seebeck coefficient of the thermoelectric material, and $\Delta T_{\mathrm{TEG}}$ is the temperature difference between the hot and cold junctions (95). This equation clearly shows that the performance of a TEG relies on the temperature gradient between the two junctions. **Figure 2*d*** depicts a representative simulation of the temperature gradient in a TEG system. For the body heat system, the hot junction is usually the human body (~36°C), and the cold junction is the ambient temperature, ranging from −10°C to 40°C.

**Figure 5*b*** presents a schematic illustration of the thermal circuit of a TEG on the human body. The temperature difference detected by the TEG is not the difference between the human

body and the ambient air. Instead, this system senses the temperature of the device surface, which is exposed to the ambient temperature, and the temperature of the skin. The difference between these surfaces is

$$\Delta T_{\mathrm{TEG}} = \frac{R_{\mathrm{TEG}}}{R_{\mathrm{air}} + R_{\mathrm{TEG}} + R_{\mathrm{body}}} \cdot \Delta T\,,$$

where the resistance ($R$) of the TEG is defined as (**Figure 5*b***) (9)

$$R_{\mathrm{TEG}} = \frac{R_{\mathrm{TE}} \cdot R_{\mathrm{fabric}}}{R_{\mathrm{TE}} + R_{\mathrm{fabric}}}.$$

Because the resistivity of ambient air and the human body is generally higher than that of a TEG, $\Delta T_{\mathrm{TEG}}$ becomes lower than the measured temperature difference between the air and the human body ($\Delta T$). Here, the output voltage is directly proportional to $\Delta T_{\mathrm{TEG}}$, and thus $\Delta T$ has a significant effect on device performance. Therefore, the performance of such devices could be improved through better design, such as increasing the number of thermocouples (95).

### 3.3. Triboelectric Generators

TENGs are made of two materials that have opposite tribopolarity (see Section 2.3). The system operates by employing the coupling effects between triboelectrification and electrostatic induction, which arise from either contact separation (**Figure 5*c***) or relative sliding (**Figure 5*d***) between two triboelectric materials (14, 96). The power generation comes from the triboelectric effect that induces electrostatic charges on the surface of the triboelectric materials and results in electron flow between the electrodes (97).

For example, in a TENG based on contact separation (96), the two triboelectric layers are polyimide (PI) and poly(methylmethacrylate) (PMMA). In the initial state, the system has no electric potential difference (EPD), because there is no generated or induced charge (**Figure 5*c,i***). The introduction of external force to the system causes the triboelectric layers to come into contact, and charge transfer occurs as a result of triboelectrification (**Figure 5*c,ii***). This transfer can be easily understood via a triboelectric series (**Figure 3**). In this example, the PI gains electrons from PMMA, which yields a net negative charge on the PI surface and a net positive charge on the PMMA surface. When the force is released, the PI film returns to its initial position due to its elasticity, leading to a layer separation and an EPD between the two electrodes (**Figure 5*c,iii***). In this state, with the assumption that the electric potential of the bottom electrode ($U_{\mathrm{BE}}$) is zero, the electric potential of the top electrode ($U_{\mathrm{TE}}$) can be defined as $U_{\mathrm{TE}} = -\sigma d'/\varepsilon_{\mathrm{o}}$, where $\sigma$, $d'$, and $\varepsilon_{\mathrm{o}}$ are the triboelectric charge density, the vacuum permittivity, and the interlayer distance, respectively. The open circuit voltage ($V_{\mathrm{oc}}$) of the system reaches its maximum when the PI film completely reverts to its initial position (**Figure 5*c,iv–v***). The application of another direct force to the system, however, causes the EPD to drop because the layers are close to one another. **Figure 5*c,vi*** shows that the $V_{\mathrm{oc}}$ falls to zero when the surface layers are in contact. This cycle continues as the triboelectric materials alternate between the contact and separation conditions due to the mechanical movements on the system.

A TENG system may also be based on in-plane sliding. This mode utilizes the sliding friction between the two materials to facilitate triboelectrification (96). **Figure 5*d*** depicts the working mechanism of this mode. In this example (98), polyamide 6,6 (nylon) and polytetrafluoroethylene (PTFE) films were chosen because they are located far from each other in the triboelectric series (**Figure 3**). Initially, the triboelectric plates are aligned and in full contact (**Figure 5*d,i***). At the interface, the triboelectrification yields a net positive charge and a net negative charge on the surfaces of nylon and PTFE, respectively, due to the large difference in their ability to attract

electrons. The lateral sliding of these two plates over each other causes a periodic change in the contact area. When the contact area decreases as the plates slide outward, the interfacial charges are separated (**Figure 5*d*,*ii***). As a result, an EPD is created between the electrodes. To compensate for the tribocharge-induced potential, a current flows from the top electrode to the bottom electrode. The current continues to flow with the ongoing sliding process until the top plate is fully out of contact from the bottom plate and the tribocharged surfaces are completely separated (**Figure 5*d*,*iii***). In this case, the current relies on the sliding velocity. When the plates slide in reverse toward their initial positions, the separated charges come into contact again. However, there is still no annihilation due to the insulator nature of polymers (**Figure 5*d*,*iv***). The redundant charges on the electrodes flow back through the external load with the increase in contact area to maintain electrostatic equilibrium. In this setting, the current flows from the bottom electrode to the top electrode. Because the plates are aligned and their surfaces are completely in contact again, there is no charge transfer between the electrodes, and the device returns to its initial state (**Figure 5*d*,*i***). The voltage generated by a TENG in in-plane sliding mode, therefore, depends on sliding displacement. With the assumption of uniform tribocharge distribution, the charge density (i.e., the total amount of transferred charge) is linearly proportional to the displacement and can be defined as $\Delta\sigma/\sigma_o = \Delta L/L_o$, where $\Delta\sigma$ is the transferred charge density, $\sigma_o$ is the tribocharge on the surface of the substrate, $\Delta L$ is the sliding displacement, and $L_o$ is the length of the plate. One can further evaluate the system's performance through the quantification of the current density ($J = d\Delta\sigma/dt$, where $t$ is time).

## 3.4. Piezoelectric Generators

The working mechanisms of piezoelectric energy harvesters are numerous and depend on the system's geometry and the type of active layer. For instance, the general working mechanism of ZnO NW energy harvesters involves the coupling between the piezoelectric and semiconducting properties of ZnO (99). Evaluation of the lateral deflection of a ZnO NW by a conductive atomic force microscope (AFM) tip provides an overview of charge and output generation in the system. In this example, a strain field arises as the ZnO NW is deflected by the AFM tip. In this state, the outer surface of the NW experiences tensile stress (positive strain), while the inner surface experiences compressive stress (negative strain). As a result, the tensile side has positive potential and the compressed side has negative potential (**Figure 5*e***). The piezoelectric potential ($V_s^+$) depends on the degree of bending of the NW and can be defined as

$$V_s^{\pm} \approx \pm 27(a/L)^3 y_m,$$

where $a$ is the radius of the NW, $L$ is the length of the NW, and $y_m$ (in nanometers) is the lateral displacement at the tip of the NW (100). Here, the Schottky barrier at the electrode–NW interface plays an important role in power generation. Evaluation of the lateral bending induced by a conductive AFM tip illustrates the charge-releasing process of the energy harvester. In this model, the NW array has a clamp-free configuration. As the AFM tip pushes the NW laterally, the NW is mechanically deflected, generating piezoelectric potential (99). The band diagram profiles of the piezoelectric NW (**Figure 5*e***) illustrate the charge output and flow process in the system. Because the NW and AFM tip have different working functions and electron affinities, there is a built-up Schottky barrier in the band diagram. In the initial state, the NW system does not have an output voltage, because it is in an equilibrium state. However, an asymmetric piezoelectric potential is generated soon after the NW is bent by the AFM tip and yields a change in the conduction band profile. This state occurs because the NW is simultaneously stretched and compressed on its lower and upper sides, respectively (**Figure 5*e***). Moreover, the local positive

piezoelectric potential is created at the tensile surface and causes an accumulation of charges in the tip because of the deceleration of electron flow from ground to tip via external load. When the AFM tip moves to the middle of the NW, the flow of accumulated electrons goes back to the ground as the local potential falls to zero. In another case, when the tip is moved to the area where the NW experiences compression, an electron flows from the *n*-type ZnO to the tip because the local negative potential elevates the conduction band profile. The overall movement of the AFM tip with respect to the NW explains the circular flow of electrons that is observed during the measurement of output current.

By contrast, the electromechanical behavior of piezoelectric thin-film membranes/ribbons can be explained through a buckling-shape model (101, 102). Here, the mechanical deformation, characterized by compression of the system at its ends, yields an out-of-plane buckling shape (**Figure 5*f***). The generated output voltage in this system is related to the strain associated with buckling. In this model, the piezoelectric material and substrate are thin-film PZT and PI, respectively. If the supporting substrate is longer than the piezoelectric membranes/ribbons, the membrane strain can be calculated as

$$\varepsilon_{\mathrm{m}} = 4\pi \frac{\overline{EI}_{\mathrm{PI}}}{\overline{EI}_{\mathrm{comp}}} \frac{h}{L} \sqrt{\frac{\Delta L}{L}},$$

where $\overline{EI}_{\mathrm{PI}}$ and $\overline{EI}_{\mathrm{comp}}$ are the plane-strain bending stiffness of the substrate (PI) without and with the piezoelectric component (PZT) and electrodes, respectively; and $h$ is the distance from the midpoint through the thickness of the PZT to the neutral mechanical plane. The voltage output that results from buckling can be further evaluated by studying the relations among stress, strain, electrical field, and electrical displacement. In this case, the output voltage of the system is defined as

$$\frac{\mathrm{d}V}{\mathrm{d}t} + \frac{N t_{\mathrm{PZT}}}{A_{\mathrm{PZT}} R \bar{k}} V = -\frac{N \bar{e} t_{\mathrm{PZT}}}{\bar{k}} \frac{\mathrm{d}\varepsilon_{\mathrm{m}}}{\mathrm{d}t},$$

where $V$ is the measured voltage, $R$ is resistance of the voltmeter, $N$ is the number of the ribbon groups electrically connected in series, $A_{\mathrm{PZT}}$ is the area of the PZT, $t_{\mathrm{PZT}}$ is the thickness of the PZT, $\bar{e}$ is the effective piezoelectric constant, and $\mathrm{d}\varepsilon_{\mathrm{m}}/\mathrm{d}t$ is the strain rate. This analytical equation suggests that the output voltage of the system is strongly dependent on the membrane strain (101).

## 4. IN VIVO EXAMPLES OF ENERGY HARVESTING FROM ANIMALS

The feasibility of generating power via energy harvesters from the human body was first investigated in animals. **Figure 6** shows representative examples of various in vivo energy harvesters (discussed above) on animal models. One type of energy harvesters that has been studied for a long time is a BFC based on the oxidation of glucose, which is present in the bloodstream (94). The feasibility of a GBFC to power implantable medical devices has been demonstrated in the abdominal cavity of a rat (**Figure 6*a***) (94). This system consists of bioelectrodes made of CNTs (see Section 2.1), modified with the GOx and laccase enzymes, which are placed in a custom-made silicon tube, wrapped in a dialysis bag, and sealed in a biocompatible Dacron® case. The total volume of this system is ~2.4 mL, and it is capable of achieving an average output voltage of 0.57 V (**Figure 6*b***) and a power density of 193.5 $\mu W/cm^2$. Thus, the output power generated by this BFC can operate a light-emitting diode (LED) or a digital thermometer (94).

In an example of mechanical energy harvesting from the motion of animal organs, Zheng et al. (103) demonstrated an implantable TENG (iTENG) based on gold, PI, PDMS, and aluminum layers with a polyethylene terephthalate spacer (103) that employs the contact separation mode described in Section 3.3. In an investigation of the potential of power generation from breathing,

an iTENG was implanted under the chest skin of a rat. The expansion and contraction of the thorax resulting from breathing yielded an average output voltage of 3.73 V. The implantation of a larger area of the iTENG onto the diaphragm of the same rat (**Figure 6*c***) demonstrated that the device can operate within the body, generating an output current of ~0.6 μA (**Figure 6*d***). These results validate the device's feasibility for use both outside and inside a rat's body.

An alternative mechanical energy harvester (MEH) that has been extensively studied is based on piezoelectric materials (**Figure 6*e–t***). One example of a piezoelectric MEH uses a PVDF film sandwiched between aluminum layers (**Figure 4*a***) to generate power from the ascending aorta of a pig (**Figure 6*e***) (74). Because PVDF is naturally flexible (see Section 2.4), it can wrap around the



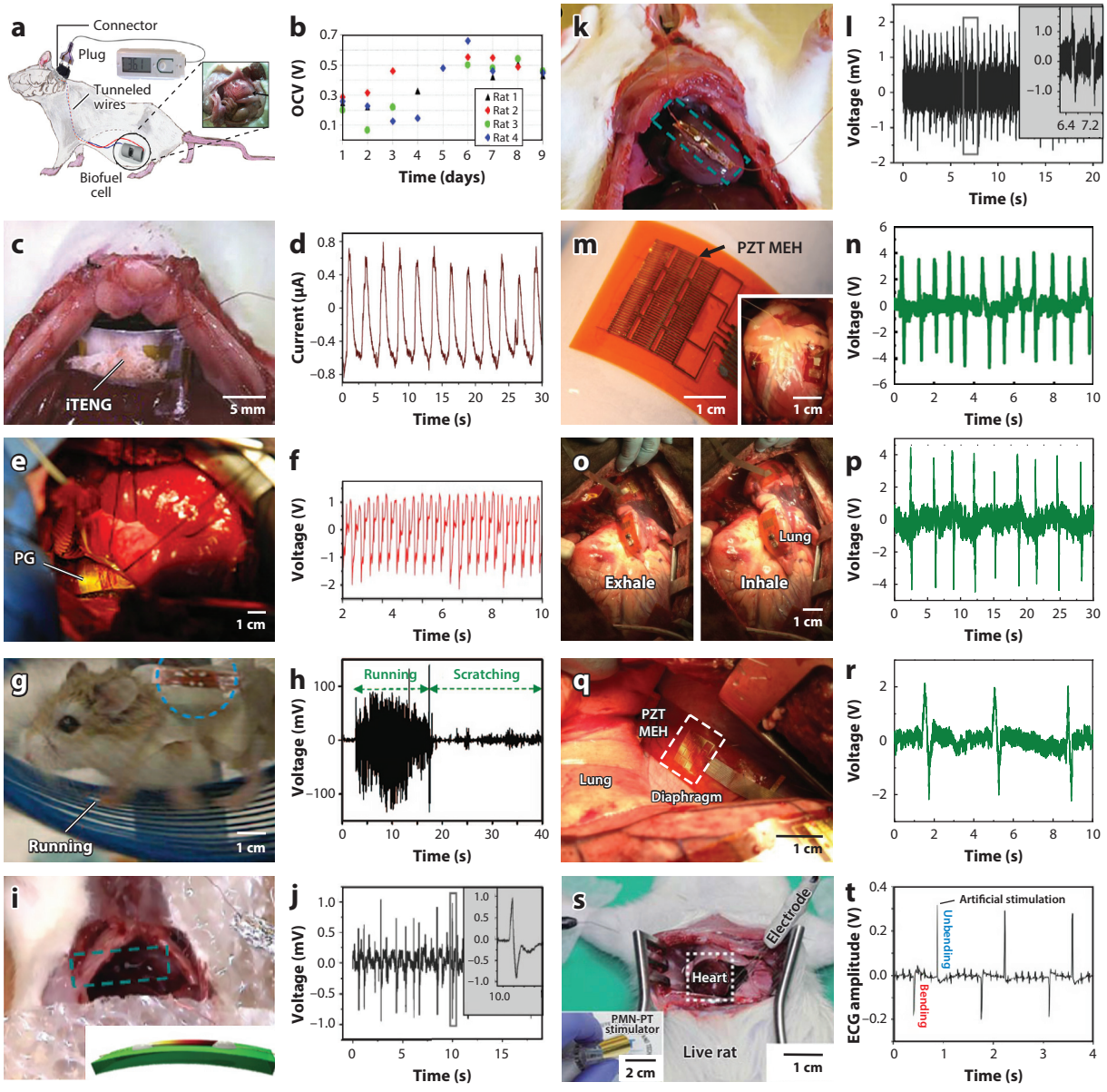

aorta and capture 10% of the variations in the diameter of the carotid artery between the systolic and diastolic states due to the pulsatile energy of the aorta (88, 89). The peak output voltage generated from this implanted system (which has dimensions of 2.5 cm × 5.6 cm × 200 μm) was 1.5 V when the heart rate and blood pressure were 120 bpm and 160/105 mm Hg, respectively (**Figure 6*f***).

A different type of piezoelectric MEH used a single-wire generator (SWG) that consists of an inorganic (e.g., ZnO) NW with its ends affixed onto a flexible substrate. The four SWGs electrically connected in series generated an output voltage in the range of ∼0.1–0.15 V. Such a system located on the back of a running hamster can generate voltages of up to 100 mV (**Figure 6*g*,*h***). According to Section 3.4, these demonstrations show that the piezoelectric SWG is sensitive enough to harvest regular and irregular biomotions (90). A further investigation of an SWG under a periodic deformation associated with the contraction and relaxation of diaphragm and heart demonstrated the possibility of using energy from internal organ movements to drive implantable devices. In this study (91), the SWG generated output voltages of ∼1 mV and 3 V, respectively, from the diaphragm (**Figure 6*i*,*j***) and heart (**Figure 6*k*,*l***) of a rat.

Another type of piezoelectric MEH utilizes PZT with a capacitor structure in a thin-film format to harvest energy from the heart, lung, and diaphragm of cow and sheep models (15). This device allows the PZT MEH to integrate with soft tissues/organs in order to capture the associated mechanical movements without placing an excessive load on them. A close examination of the implanted device positioned on a heart suggests that placement on the right ventricle (RV) and a 45° orientation of the PZT ribbons with respect to the apex of the heart are the optimal configuration to harness maximum power. By use of the concept discussed in Section 3.4, output voltages of ∼4 V, ∼4 V, and ∼2 V, respectively, were generated from contraction and relaxation of the RV (**Figure 6*m*,*n***), lung (**Figure 6*o*,*p***), and diaphragm (**Figure 6*q*,*r***). Additionally, a stack of five PZT MEHs can generate a power density of 1.2 μW/cm$^2$. These results show that the device is able to power implantable devices, particularly a cardiac pacemaker (15).

Because the motions of the heart present a great opportunity for energy harvesting, many researchers have focused on improving device performance by utilizing various piezoelectric materials. One of these is PMN-PT due to its high piezoelectric constant. Hwang et al. (86) fabricated a flexible thin-film PMN-PT energy harvester (with dimensions of 1.7 cm × 1.7 cm) that not only can acquire energy from the heart but also can serve as an artificial heart stimulator. **Figure 6*s*** shows this device being implanted into the heart of a rat in order to examine its feasibility. This

**Figure 6**

In vivo demonstrations of energy harvesters on various animal models. (*a*) A glucose biofuel cell implanted in an abdominal cavity of a Wistar rat. (*Inset*) The biofuel cell after 17 days (94). (*b*) The open-circuit voltage (OCV) outputs of the biofuel cells implanted into four rats over 9 days (94). (*c*) A photograph of an implantable triboelectric nanogenerator (iTENG) on the diaphragm of a rat (103). (*d*) The output current generated from the diaphragm of a rat (103). (*e*) A photograph of an implanted piezoelectric generator (PG) made of polyvinylidene fluoride (PVDF) placed on the ascending aorta of a pig. The PG is sealed with polyimide (PI) tape (74). (*f*) The corresponding output voltage generated from the ascending aorta of a pig (74). (*g*) A photograph of a running hamster with an implanted single-wire generator (SWG) (90). (*h*) The corresponding output voltage when the hamster was running and scratching (90). (*i*) A photograph of an SWG implanted on the diaphragm of a rat (91). (*j*) The generated output voltage from the diaphragm motion (91). (*k*) A photograph of an SWG implanted onto the heart of a rat (91). (*l*) The output voltage generated from the heartbeats (91). (*m*) A photograph of a flexible lead zirconate titanate mechanical energy harvester (PZT MEH). (*Inset*) The MEH affixed onto a cow heart (15). (*n*) The output voltage generated from the MEH affixed onto the right ventricle of a cow heart (15). (*o*) A photograph of the PZT MEH on a cow lung (15). (*p*) The associated output voltage generated from the lung motions (15). (*q*) A photograph of the PZT MEH implanted onto a cow diaphragm (15). (*r*) The associated output voltage generated from the diaphragm motions (15). (*s*) A photograph of a flexible $(1 - x)Pb(Mg_{1/3}Nb_{2/3})O_3 - xPbTiO_3$ (PMN-PT) energy harvester used to stimulate the heart of a rat. (*Inset*) The PMN-PT stimulator (86). (*t*) The electrocardiogram (ECG) voltage resulting from the artificial stimulations (86).

PMN-PT nanogenerator can generate an output voltage of 8.2 V from a strain of 0.36% at a strain rate of 2.3%/s and can stimulate the heart with the electrical power generated from the motions of the heart (**Figure 6*t***).

## 5. IN VIVO EXAMPLES OF ENERGY HARVESTING FROM HUMANS

The advances in energy harvesters on animal models described in the previous section provide a foundation for these devices' projected use on or in the human body. Recent studies reveal a wide range of energy harvesters capable of generating power, particularly in wearable configurations such as wristbands, bracelets, and clothing.

As noted in Section 2.1, sweat lactate and its associated enzyme represent a way to generate electricity via a BFC. The integration of a BFC and a printed circuit board with a fabric textile substrate imparts flexibility to the system (23). These textile-based BFCs are fabricated via screen-printing techniques on a detachable care label through use of thick-film printing technology, which has the advantage of high-scale, low-cost production (104, 105). BFCs made with this technique (**Figure 7*a***) can be readily incorporated into various garments, such as headbands and wristbands. **Figure 7*b*** shows the output profiles of a BFC at various lactate fuel concentrations, ranging from 3 to 21 mM in 0.1 M phosphate buffer. These results reveal the capability of this BFC to generate power with linear proportionality to the fuel concentration. Specifically, the BFC can generate an open circuit potential of 0.67 V and a power density of 100 $\mu W/cm^2$ (electrode area of $3 \times 1.5$ $mm^2$) when it is exposed to 15 mM lactate. Thus, this BFC can light up a blue LED and power a watch, demonstrating its promising applications in customized wearable electronics.

TEGs are also of interest because they take advantage of the heat that is continuously generated from the human body (described in detail in Sections 2.2 and 3.2). **Figure 7*c*** shows an example of a functional thermoelectric energy harvester based on SiGe that is fabricated via stepper lithography (described in Section 2.2) (50). **Figure 7*d*** depicts the ability of such a system to harvest energy from various temperature differences. An output voltage ranging from 0.15 V to 0.70 V can be expressed as a function of the difference between the high-temperature area and the ambient

**Figure 7**

In vivo demonstrations of energy harvesters on various parts of the human body. (*a*) (*i*) A photograph of a textile biofuel cell (BFC) integrated into various wearable items, such as headbands or wristbands. (*ii*) A scheme of the textile BFC, including a bioanode for lactate oxidation and a cathode for oxygen reduction. (*iii*) A customized printed circuit board prototype for the conversion, conditioning, and temporary storage of extracted energy (23). (*b*) The power density of the textile BFC at varying lactate fuel concentrations (3–21 mM) in 0.1 M phosphate buffer (23). (*c*) A photograph of a wearable wireless electroencephalogram (EEG) system with a thermoelectric-photovoltaic power supply wrapped around a human head (50). (*d*) The voltage output of the thermoelectric device (50). (*e*) A photograph of a prototype flex circuit integrated onto the bracelet of a thermoelectric generator (TEG) to power a wristwatch (106). (*f*) The open circuit voltage generated by a TEG used indoors when (*i*) sitting quietly, (*ii*) doing normal activity, and (*iii*) walking at a speed of ~4 km/h (106). (*g*) A photograph of an integrated self-charging power system that harvests mechanical energy from human motion with triboelectric nanogenerator (TENG) cloth, stores the energy with a lithium-ion battery (LIB) belt, and then powers a heartbeat-meter strap, which has remote communication with a smartphone (107). (*h*) The open circuit voltage generated by the TENG. An individual voltage peak between 0 and 1 s is shown, with the associated pressing and releasing steps (107). (*i*) A photograph of a backpack integrated with a rhombic gridding TENG, which can light 40 commercial light-emitting diode (LED) bulbs simultaneously (108). (*j*) The open circuit voltage generated by a rhombic gridding–based TENG (108). (*k*) A photograph of a woven structured TENG (W-TENG) integrated into the sole of a shoe (109). (*l*) The associated current generated by the W-TENG under the shoe (109). (*m*) A photograph of the W-TENG integrated with a trouser at the leg joint (109). (*n*) The associated current generated by the W-TENG at the leg joint (109). (*o*) Scanning electron microscope images and a schematic illustration of a stretchable energy harvester composed of highly ordered zinc oxide/lead zirconate titanate (ZnO/PZT) hollow hemispheres (79). (*p*) The corresponding output voltages of the energy harvester generated during upward and downward hand motions (79).

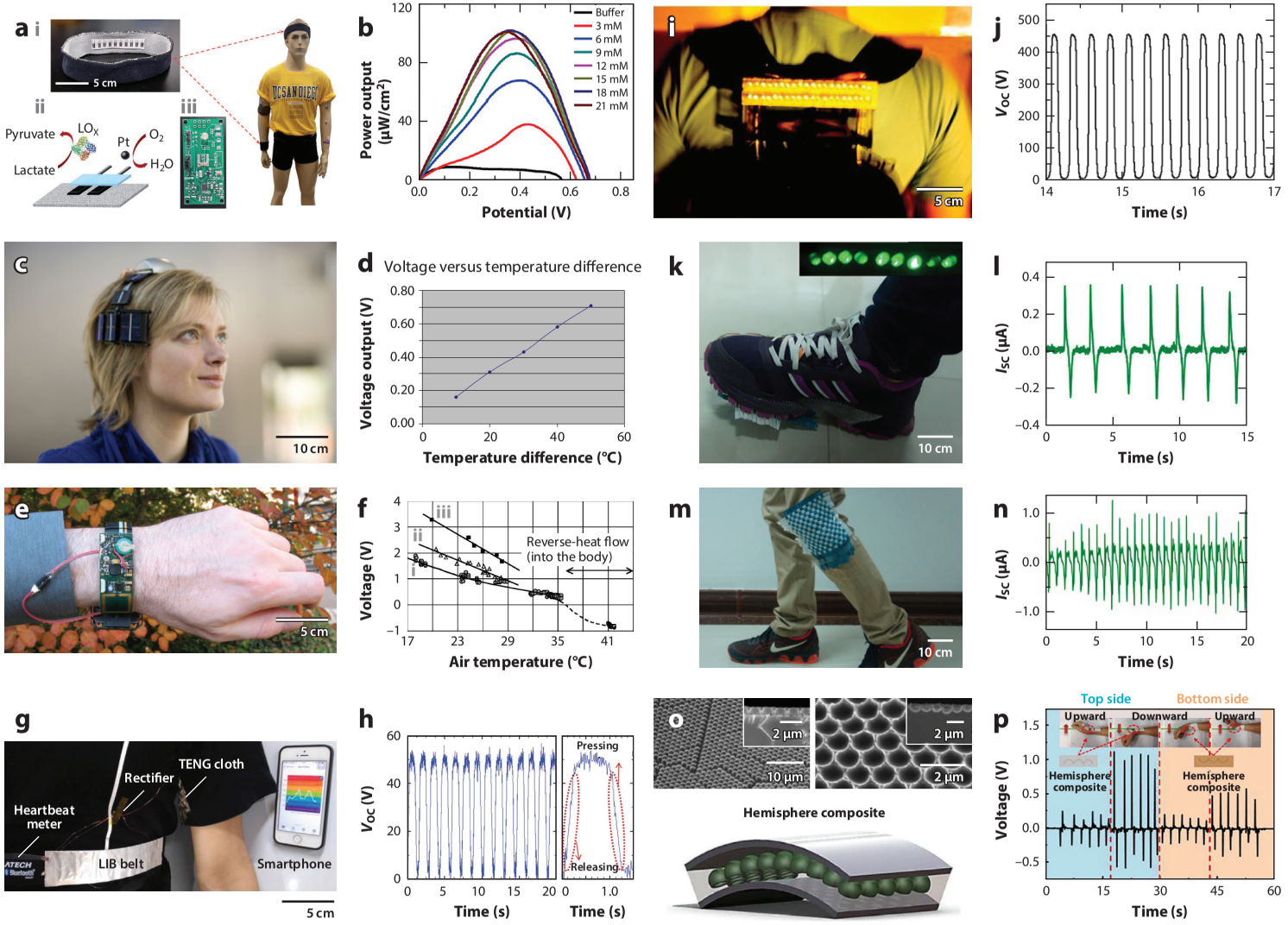

temperature of 22°C; this result demonstrates the functionality of the system over a wide range of temperatures. Another type of TEGs is based on BiTe thermopiles; BiTe is the intermediate state of $Bi_2Te_3$ (described in Section 2.2). The system can be worn as a bracelet to utilize the dissipated heat from the human body to power a wristwatch (**Figure 7*e***). This TEG can also capture energy from the temperature difference between various activities, such as sitting quietly and walking, and can generate the output voltages shown in **Figure 7*f*** (106). In addition, the BiTe TEG can reliably operate at indoor ambient temperatures and can generate an average power of approximately 250 μW during the daytime. This value corresponds to approximately 20 $\mu W/cm^2$, enabling the use of this device to power wearable electronics.

Mechanical energy harvesting via a TENG is appealing due to its low cost, environmental friendliness, and universal availability, as well as its remarkable capability to generate power from human movements. Pu et al. (107) developed an integrated textile TENG cloth with a flexible lithium-ion battery (LIB) belt (**Figure 7*g***). The TENG cloth has the flexibility needed for use at various locations on the human body, and the LIB belt serves as an energy storage device. Utilizing the contact separation triboelectrification mode described in Section 3.3, the TENG cloth (with dimensions of $5 \times 5$ $cm^2$) has an output circuit voltage of ~50 V (**Figure 7*h***). This system can charge the LIB belt to the operational voltage of ~1.9 V with three cycles of triboelectrification and can power a heartbeat meter strap that uses Bluetooth technology to wirelessly communicate with a smartphone.

Another study demonstrated the application of a TENG in a self-powered backpack configuration, which harvests the vibration energy from walking (**Figure 7*i***). In this study (108), the construction of a TENG involved rhombic gridding employing multiple unit cells in order to enhance the output voltage of the system. In addition to the multiple unit cells, the combination of contact separation and sliding electrification (see Section 3.3) enabled the system to achieve an open circuit voltage of 428 V (**Figure 7*j***), with a peak power density of 30.7 $W/m^2$ (on a system with three unit cells). Such a rhombic gridding TENG can light up 40 LEDs when a person walks naturally while carrying the backpack (a total weight of 2.0 kg). These results show that TENGs can harness vibration energy from a walking human to potentially extend the lifetime of a battery or even to build self-powered systems.

An alternative way to use both the contact separation and lateral sliding modes involves the fabrication of a woven structured TENG (W-TENG). A W-TENG employs nylon fabric and polyester fabric as the triboelectric surfaces, which are located far apart from one another in the triboelectric series (**Figure 3**), and conductive silver fiber fabric as the electrode (109). A freestanding W-TENG can generate an open circuit voltage of 90 V under 12 mm displacement. A W-TENG (with an effective area of 20 $cm^2$) has been placed onto the bottom of a shoe to harvest the energy from footsteps and light up nine LEDs, generating an output current of ~0.3 μA (**Figure 7*k*,*l***). This W-TENG can also be integrated into trouser fabric to harvest mechanical energy from joint movement (**Figure 7*k***). The integration of such systems with clothing can generate an output current of ~0.9 μA (**Figure 7*l***). These results demonstrate the potential application of W-TENGs on various parts of the human body to harvest mechanical energy from movement for use in wearable electronics.

MEHs based on inorganic piezoelectric materials have also been extensively discussed. As discussed in Section 2.4, inorganic piezoelectric materials (e.g., ZnO and PZT) are brittle, but this limitation can be overcome through the construction of a thin film made of a highly ordered piezoelectric hemisphere embedded in a PDMS matrix (**Figure 7*o***) (79). Such hemisphere structures not only exhibit elastic deformation upon the application and release of external forces, but also allow simultaneous and stable output power generation. These systems can generate an output voltage of ~1.1 V from bending/stretching deformations introduced by upward and downward

hand motions (**Figure 7*p***). Furthermore, this system can achieve an output voltage of 6 V through a stack of three hemisphere layers under a strain of ~0.425%. The high output voltage generation, along with the flexibility and stretchability of the energy harvester, offers a strong foundation for wearable devices.

## 6. CONCLUSIONS AND OUTLOOK

Despite their improved battery capacity and reduced power demand, power sources for wearable/implantable devices still require frequent battery replacements. As a result, patients have to undergo multiple surgical procedures, with associated health risks (and high costs, in the case of implantable devices). Energy harvesting from living subjects, as a means to recharge a battery or to supply power without the need for batteries, is a promising solution to this problem. From among the various energy harvesting approaches, we have described only the most extensively studied ones based on BFCs, thermoelectricity, triboelectricity, and piezoelectricity. We have also explained the essential working principles of these energy harvesters, along with key considerations in their designs and material selection. We have summarized several representative in vivo demonstrations on various animal and human models.

Energy harvesting from living subjects will continue to advance in the future, with a focus on building self-powered electronics, especially for biomedical applications. First, it is important to improve the output power and efficiency of the energy harvesters so that they can be sufficient to power electronics sustainably. Second, it is important to ensure the devices' biocompatibility. Third, the stability and robustness of energy harvesters must be improved so that their lifetime is longer than that of a battery. Finally, because some existing energy harvesters are built on rigid electronics, these systems should be reconfigured so that they can integrate with soft biological tissues.

Advances in materials science, mechanical engineering, and fabrication techniques have facilitated the development of electronic devices into mechanically adaptive forms. A prospective research direction would be to further combine advanced engineering principles with existing energy harvesters. The integration of various energy harvesters with advanced electronics could open new routes to develop novel technologies for disease diagnostics, treatment, and prevention.

## DISCLOSURE STATEMENT

The authors are not aware of any affiliations, memberships, funding, or financial holdings that might be perceived as affecting the objectivity of this review.

## ACKNOWLEDGMENTS

C.D. thanks Pauline Joe for her participation in the literature search and contribution to manuscript writing. C.D. acknowledges Prof. John A. Rogers of the University of Illinois at Urbana-Champaign and Prof. Robert S. Langer of the David H. Koch Institute for Integrative Cancer Research at Massachusetts Institute of Technology for their valuable guidance. C.D. also acknowledges the Society of Fellows of Harvard University for financial support. Z.L.W. is grateful for support from the National Science Foundation (grant DMR-1505319); the US Department of Energy, Office of Basic Energy Sciences (award DE-FG02-07ER46394); King Abdullah University of Science and Technology; the Hightower Chair Foundation; and the "Thousand Talents" Program for the Pioneer Researcher and His Innovation Team, National Natural Science Foundation of China (grants 51432005, 5151101243, and 51561145021).

## LITERATURE CITED

1. Patel S, Park H, Bonato P, Chan L, Rodgers M. 2012. A review of wearable sensors and systems with application in rehabilitation. *J. Neuroeng. Rehabil.* 9:21–47
2. Joung YH. 2013. Development of implantable medical devices: from an engineering perspective. *Int. Neurourol. J.* 17:98–106
3. Bandodkar A, Wang J. Non-invasive wearable electrochemical sensors: a review. *Trends Biotechnol.* 32:363–71
4. Mallela VS, Ilankumaran V, Rao NS. 2004. Trends in cardiac pacemakers batteries. *Indian Pacing Electrophysiol. J.* 4:201–12
5. Riemer R, Shapiro A. 2011. Biomechanical energy harvesting from human motion: theory, state of the art, design guidelines, and future directions. *J. Neuroeng. Rehabil.* 8:22
6. Hannan M, Mutashar S, Samad S, Hussain A. 2014. Energy harvesting for implantable medical devices: issues and challenges. *Biomed. Eng. Online* 13:79–101
7. Halámková L, Halámek J, Bocharova V, Szczupak A, Alfonta L, Katz E. 2012. Implanted biofuel cell operating in a living snail. *J. Am. Chem. Soc.* 134:5040–43
8. Starner T. 1996. Human-powered wearable computing. *IBM Syst. J.* 35:618–29
9. Vuller RJM, van Schaijk R, Doms I, Van Hoof C, Mertens R. 2009. Micropower energy harvesting. *Solid State Electron.* 53:684–93
10. Sue CY, Tsai NC. 2012. Human powered MEMS-based energy harvest devices. *Appl. Energy* 93:390–403
11. Mercier PP, Lysaght AC, Bandyopadhyay S, Chandrakasan AP, Stankovic KM. 2012. Energy extraction from the biologic battery in the inner ear. *Nat. Biotechnol.* 30:1240–43
12. Leonov V, Vullers RJM. 2009. Wearable thermoelectric generators for body-powered devices. *J. Electron. Mater.* 38:1491–98
13. Ramadass YK, Chandrakasan AP. 2011. A battery-less thermoelectric energy harvesting interface circuit with 35 mV startup voltage. *IEEE J. Solid-State Circuits* 46:333–41
14. Wang ZL. 2013. Triboelectric nanogenerators as new energy technology for self-powered systems and as active mechanical and chemical sensors. *ACS Nano* 7:9533–57
15. Dagdeviren C, Yang BD, Su Y, Tran PL, Joe P, et al. 2014. Conformal piezoelectric energy harvesting and storage from motions of the heart, lung, and diaphragm. *PNAS* 111:1927–32
16. Renaud M, Fiorini P, van Schaijk R, van Hoof C. 2012. Harvesting energy from the motion of human limbs: the design and analysis of an impact-based piezoelectric generator. *Smart Mater. Struct.* 21:049501
17. Lee M, Chen C-Y, Wang S, Cha SN, Park YJ, et al. 2012. A hybrid piezoelectric structure for wearable nanogenerators. *Adv. Mater.* 24:1759–64
18. Dagdeviren C, Hwang S-W, Su Y, Kim S, Cheng H, et al. 2013. Transient, biocompatible electronics and energy harvesters based on ZnO. *Small* 9:3398–404
19. Barton SC, Gallaway J, Atanassov P. 2004. Enzymatic biofuel cells for implantable and microscale devices. *Chem. Rev.* 104:4867–86
20. Heller A. 2004. Miniature biofuel cells. *Phys. Chem. Chem. Phys.* 6:209–16
21. Hansen BJ, Liu Y, Yang R, Wang ZL. 2010. Hybrid nanogenerator for concurrently harvesting biomechanical and biochemical energy. *ACS Nano* 4:3647–52
22. Katz E, MacVittie K. 2013. Implanted biofuel cells operating in vivo—methods, applications and perspectives. *Energy Environ. Sci.* 6:2791–803
23. Jia W, Wang X, Imani S, Bandodkar AJ, Ramírez J, et al. 2014. Wearable textile biofuel cells for powering electronics. *J. Mater. Chem. A* 2:18184–89
24. Wilson R, Turner APF. 1992. Glucose oxidase: an ideal enzyme. *Biosens. Bioelectron.* 7:165–85
25. Cinquin P, Gondran C, Giroud F, Mazabrard S, Pellissier A, et al. 2010. A glucose biofuel cell implanted in rats. *PLOS ONE* 5:e10476
26. Sales FCPF, Iost RM, Martins MVA, Almeida MC, Crespilho FN. 2013. An intravenous implantable glucose/dioxygen biofuel cell with modified flexible carbon fiber electrodes. *Lab Chip* 13:468–74
27. Milton RD, Giroud F, Thumser AE, Minteer SD, Slade RCT. 2013. Hydrogen peroxide produced by glucose oxidase affects the performance of laccase cathodes in glucose/oxygen fuel cells: FAD-dependent glucose dehydrogenase as a replacement. *Phys. Chem. Chem. Phys.* 15:19371–79

28. Narváez Villarrubia CW, Rincón RA, Radhakrishnan VK, Davis V, Atanassov P. 2011. Methylene green electrodeposited on SWNTs-based "bucky" papers for NADH and L-malate oxidation. *ACS Appl. Mater. Interfaces* 3:2402–9
29. Zayats M, Katz E, Willner I. 2002. Electrical contacting of flavoenzymes and $NAD(P)^+$-dependent enzymes by reconstitution and affinity interactions on phenylboronic acid monolayers associated with Au-electrodes. *J. Am. Chem. Soc.* 124:14724–35
30. Cosnier S, Le Goff A, Holzinger M. 2013. Towards glucose biofuel cells implanted in human body for powering artificial organs: review. *Electrochem. Commun.* 38:19–23
31. Szczupak A, Halámek J, Halámková L, Bocharova V, Alfonta L, Katz E. 2012. Living battery-biofuel cells operating in vivo in clams. *Energy Environ. Sci.* 5:8891–95
32. MacVittie K, Halámek J, Halámková L, Southcott M, Jemison WD, et al. 2013. From "cyborg" lobsters to a pacemaker powered by implantable biofuel cells. *Energy Environ. Sci.* 6:81–86
33. Castorena-Gonzalez JA, Foote C, MacVittie K, Halámek J, Halámková L, et al. 2013. Biofuel cell operating in vivo in rat. *Electroanalysis* 25:1579–84
34. Meredith MT, Minteer SD. 2012. Biofuel cells: enhanced enzymatic bioelectrocatalysis. *Annu. Rev. Anal. Chem.* 5:157–79
35. Atanassov P, Apblett C, Banta S, Brozik S, Barton SC, et al. 2007. Enzymatic biofuel cells. *Electrochem. Soc. Interface* 16:28–52
36. Yu EH, Scott K. 2010. Enzymatic biofuel cells—fabrication of enzyme electrodes. *Energies* 3:23–42
37. Hu L, Hecht DS, Grüner G. 2010. Carbon nanotube thin films: fabrication, properties, and applications. *Chem. Rev.* 110:5790–844
38. Fuchsberger K, Goff AL, Gambazzi L, Toma FM, Goldoni A, et al. 2011. Multiwalled carbon-nanotube-functionalized microelectrode arrays fabricated by microcontact printing: platform for studying chemical and electrical neuronal signaling. *Small* 7:524–30
39. Gooding JJ. 2005. Nanostructuring electrodes with carbon nanotubes: a review on electrochemistry and applications for sensing. *Electrochim. Acta* 50:3049–60
40. Hughes M, Chen GZ, Shaffer MSP, Fray DJ, Windle AH, et al. 2002. Electrochemical capacitance of a nanoporous composite of carbon nanotubes and polypyrrole. *Chem. Mater.* 14:1610–13
41. Holzinger M, Le Goff A, Cosnier S. 2012. Carbon nanotube/enzyme biofuel cells. *Electrochim. Acta* 82:179–90
42. Leonov V. 2011. Human machine and thermoelectric energy scavenging for wearable devices. *ISRN Renew. Energy* 2011:785380
43. Chung DY, Hogan T, Brazis P, Rocci-Lane M, Kannewurf C, et al. 2000. $CsBi_4Te_6$: a high-performance thermoelectric material for low-temperature applications. *Science* 287:1024–27
44. Poudel B, Hao Q, Ma Y, Lan Y, Minnich A, et al. 2008. High-thermoelectric performance of nanostructured bismuth antimony telluride bulk alloys. *Science* 320:634–38
45. Liu W, Lukas KC, McEnaney K, Lee S, Zhang Q, et al. 2013. Studies on the $Bi_2Te_3$–$Bi_2Se_3$–$Bi_2S_3$ system for mid-temperature thermoelectric energy conversion. *Energy Environ. Sci.* 6:552–60
46. Sun Y, Cheng H, Gao S, Liu Q, Sun Z, et al. 2012. Atomically thick bismuth selenide freestanding single layers achieving enhanced thermoelectric energy harvesting. *J. Am. Chem. Soc.* 134:20294–97
47. Zhao LD, Lo SH, Zhang Y, Sun H, Tan G, et al. 2014. Ultralow thermal conductivity and high thermoelectric figure of merit in SnSe crystals. *Nature* 508:373–77
48. Heremans JP, Jovovic V, Toberer ES, Saramat A, Kurosaki K, et al. 2008. Enhancement of thermoelectric efficiency in PbTe by distortion of the electronic density of states. *Science* 321:554–57
49. Delaire O, Ma J, Marty K, May AF, McGuire MA, et al. 2011. Giant anharmonic phonon scattering in PbTe. *Nat. Mater.* 10:614–19
50. Su J, Vullers RJM, Goedbloed M, van Andela Y, Leonovb V, Wang Z. 2010. Thermoelectric energy harvester fabricated by Stepper. *Microelectron. Eng.* 87:1242–44
51. Liu J, Zhang LM, He L, Tang XF. 2008. Synthesis and thermoelectric properties of polyaniline. *J. Wuhan Univ. Technol. Mater. Sci. Ed.* 18:53–55
52. Lee K, Cho S, Park SH, Heeger AJ, Lee CW, Lee SH. 2006. Metallic transport in polyaniline. *Nature* 441:65–68

53. Kemp NT, Kaiser AB, Liu CJ, Chapman B, Mercier O, et al. 1999. Thermoelectric power and conductivity of different types of polypyrrole. *J. Polym. Sci. B* 37:953–60
54. Eftekhari A, Kazemzad M, Keyanpour-Rad M. 2006. Significant effect of dopant size on nanoscale fractal structure of polypyrrole film. *Polym. J.* 38:781–85
55. Nardes AM, Kemerink M, Janssen RAJ, Bastiaansen JAM, Kiggen NMM, et al. 2007. Microscopic understanding of the anisotropic conductivity of PEDOT: PSS thin films. *Adv. Mater.* 19:1196–200
56. Park T, Park C, Kim B, Shin H, Kim E. 2013. Flexible PEDOT electrodes with large thermoelectric power factors to generate electricity by the touch of fingertips. *Energy Environ. Sci.* 6:788–92
57. Bubnova O, Khan ZU, Malti A, Braun S, Fahlman M, et al. 2011. Optimization of the thermoelectric figure of merit in the conducting polymer poly(3,4-ethylenedioxythiophene). *Nat. Mater.* 10:429–33
58. Sun Y, Sheng P, Di C, Jiao F, Xu W, et al. 2012. Organic thermoelectric materials and devices based on *p*- and *n*-type poly(metal 1,1,2,2-ethenetetrathiolate)s. *Adv. Mater.* 24:932–37
59. Kim SJ, We JH, Cho BJ. 2014. A wearable thermoelectric generator fabricated on a glass fabric. *Energy Environ. Sci.* 7:1959–65
60. Dun C, Hewitt CA, Huang H, Xu J, Zhou C, et al. 2015. Flexible *n*-type thermoelectric films based on Cu-doped $Bi_2Se_3$ nanoplate and polyvinylidene fluoride composite with decoupled Seebeck coefficient and electrical conductivity. *Nano Energy* 18:306–14
61. Wang ZL, Chen J, Lin L. 2015. Progress in triboelectric nanogenerators as a new energy technology and self-powered sensors. *Energy Environ. Sci.* 8:2250–82
62. Fan X, Chen J, Yang J, Bai P, Li Z, Wang ZL. 2015. Ultrathin, rollable, paper-based triboelectric nanogenerator for acoustic energy harvesting and self-powered sound recording. *ACS Nano* 9:4236–43
63. Lin Z, Cheng G, Li X, Yang PK, Wen X, Wang ZL. 2015. A multi-layered interdigitative-electrodes-based triboelectric nanogenerator for harvesting hydropower. *Nano Energy* 15:256–65
64. Jing Q, Xie Y, Zhu G, Han RPS, Wang ZL. 2015. Self-powered thin-film motion vector sensor. *Nat. Commun.* 6:1–8
65. Fan F, Lin L, Zhu G, Wu W, Zhang R, Wang ZL. 2012. Transparent triboelectric nanogenerators and self-powered pressure sensors based on micropatterned plastic films. *Nano Lett.* 12:3109–14
66. Zhong X, Yang Y, Wang X, Wang ZL. 2015. Rotating-disk-based hybridized electromagnetic-triboelectric nanogenerator for scavenging biomechanical energy as a mobile power source. *Nano Energy* 13:771–80
67. Lin Z, Xie Y, Yang Y, Wang S, Zhu G, Wang ZL. 2013. Enhanced triboelectric nanogenerators and triboelectric nanosensor using chemically modified $TiO_2$ nanomaterials. *ACS Nano* 7:4554–60
68. Yang J, Chen J, Su Y, Jing Q, Li Z, et al. 2015. Eardrum-inspired active sensors for self-powered cardiovascular system characterization and throat-attached anti-interference voice recognition. *Adv. Mater.* 27:1316–26
69. Lin L, Xie Y, Niu S, Wang S, Yang PK, Wang ZL. 2015. Robust triboelectric nanogenerator based on rolling electrification and electrostatic induction at an instantaneous energy conversion efficiency of ~55%. *ACS Nano* 9:922–30
70. Yang W, Chen J, Wen X, Jing Q, Yang J, et al. 2014. Triboelectrification based motion sensor for human–machine interfacing. *ACS Appl. Mater. Interfaces* 6:7479–84
71. Wang ZL, Wu W. 2012. Nanotechnology-enabled energy harvesting for self-powered micro-/nanosystems. *Angew. Chem. Int. Ed.* 51:2–24
72. Koo JH, Seo J, Lee T. 2012. Nanomaterials on flexible substrates to explore innovative functions: from energy harvesting to bio-integrated electronics. *Thin Solid Films* 524:1–19
73. Persano L, Catellani A, Dagdeviren C, Ma Y, Guo X, et al. 2016. Shear piezoelectricity in poly(vinylidenefluoride-*co*-trifluoroethylene): full piezotensor coefficients by molecular modeling, biaxial transverse response, and use in suspended energy-harvesting nanostructures. *Adv. Mater.* 28:7633–39
74. Zhang H, Zhang X-S, Cheng X, Liu Y, Han M, et al. 2015. A flexible and implantable piezoelectric generator harvesting energy from the pulsation of ascending aorta: in vitro and in vivo studies. *Nano Energy* 12:296–304
75. Cheng X, Xue X, Ma Y, Han M, Zhang W, et al. 2016. Implantable and self-powered blood pressure monitoring based on a piezoelectric thin film: simulated, in vitro and in vivo studies. *Nano Energy* 22:453–60

76. Dagdeviren C, Joe P, Tuzman OL, Park K-I, Lee KJ, et al. 2016. Recent progress in flexible and stretchable piezoelectric devices for mechanical energy harvesting, sensing and actuation. *Extreme Mech. Lett.* 9:269–91
77. Dagdeviren C. 2015. *Ferroelectric/piezoelectric flexible mechanical energy harvesters and stretchable epidermal sensors for medical applications*. PhD thesis, Dep. Mater. Sci. Eng., Univ Ill., Urbana-Champaign
78. Alkoy EM, Dagdeviren C, Papila M. 2008. $Pb(Zr,Ti)O_3$ nanofibers produced by electrospinning process. *Mater. Res. Soc. Symp. Proc.* 1129:V7–8
79. Chun J, Kang N-R, Kim J-Y, Noh M-S, Kang C-Y, et al. 2015. Highly anisotropic power generation in piezoelectric hemispheres composed stretchable composite film for self-powered motion sensor. *Nano Energy* 11:1–10
80. Chen X, Xu S, Yao N, Shi Y. 2010. 1.6 V nanogenerator for mechanical energy harvesting using PZT nanofibers. *Nano Lett.* 10:2133–37
81. Park K-I, Son JH, Hwang GT, Jeong CK, Ryu J, et al. 2014. Highly-efficient, flexible piezoelectric PZT thin film nanogenerator on plastic substrates. *Adv. Mater.* 26:2514–20
82. Park K-I, Lee M, Liu Y, Moon S, Hwang G-T, et al. 2012. Flexible nanocomposite generator made of $BaTiO_3$ nanoparticles and graphitic carbons. *Adv. Mater.* 24:2999–3004
83. Choi MY, Choi D, Jin MJ, Kim I, Kim SH, et al. 2009. Mechanically powered transparent flexible charge-generating nanodevices with piezoelectric ZnO nanorods. *Adv. Mater.* 21:2185–89
84. Wang ZL, Zhu G, Yang Y, Wang SH, Pan CF. 2012. Progress in nanogenerators for self-powered mobile/portable electronics. *Mater. Today* 15:532–43
85. Zhu G, Yang R, Wang S, Wang ZL. 2010. Flexible high-output nanogenerator based on lateral ZnO nanowire array. *Nano Lett.* 10:3151–55
86. Hwang GT, Park H, Lee J-H, Oh S, Park K-I, et al. 2014. Self-powered cardiac pacemaker enabled by flexible single crystalline PMN-PT piezoelectric energy harvester. *Adv. Mater.* 26:4880–87
87. Cheng L, Yuan M, Gu L, Wang Z, Qin Y, et al. 2015. Wireless, power-free and implantable nanosystem for resistance-based biodetection. *Nano Energy* 15:598–606
88. Dammers R, Stifft F, Tordoir JH, Hameleers JM, Hoeks AP, Kitslaar PJ. 2003. Shear stress depends on vascular territory: comparison between common carotid and brachial artery. *J. Appl. Physiol.* 94:485–89
89. Bussy C, Boutouyrie P, Lacolley P, Challande P, Laurent S. 2000. Intrinsic stiffness of the carotid arterial wall material in essential hypertensives. *Hypertension* 35:1049–54
90. Yang R, Qin Y, Li C, Zhu G, Wang ZL. 2009. Converting biomechanical energy into electricity by a muscle-movement driven nanogenerator. *Nano Lett.* 9:1201–5
91. Li Z, Zhu G, Yang R, Wang AC, Wang ZL. 2010. Muscle-driven in vivo nanogenerator. *Adv. Mater.* 22:2534–37
92. Mano N, Mao F, Heller A. 2003. Characteristics of a miniature compartment-less glucose/$O_2$ biofuel cell and its operation in a living plant. *J. Am. Chem. Soc.* 125:6588–94
93. Rapoport BI, Kedzierski JT, Sarpeshkar R. 2012. A glucose fuel cell for implantable brain–machine interfaces. *PLOS ONE* 7:e38436
94. Zebda A, Cosnier S, Alcaraz J-P, Holzinger M, Le Goff A, et al. 2013. Single glucose biofuel cells implanted in rats power electronic devices. *Sci. Rep.* 3:1516
95. Kim MK, Kim MS, Lee S, Kim C, Kim YJ. 2014. Wearable thermoelectric generator for harvesting human body heat energy. *Smart Mater. Struct.* 23:105002
96. Zhu G, Pan C, Guo W, Chen CY, Zhou Y, et al. 2012. Triboelectric-generator-driven pulse electrodeposition for micropatterning. *Nano Lett.* 12:4960–65
97. Hou TC, Yang Y, Zhang H, Chen J, Chen LJ, Wang ZL. 2013. Triboelectric nanogenerator built inside shoe insole for harvesting walking energy. *Nano Energy* 2:856–62
98. Wang S, Lin L, Xie Y, Jing Q, Niu S, Wang ZL. 2013. Sliding-triboelectric nanogenerators based on in-plane charge-separation mechanism. *Nano Lett.* 13:2226–33
99. Wang ZL. 2008. Towards self-powered nanosystems: from nanogenerators to nanopiezotronics. *Adv. Funct. Mater.* 18:3553–67
100. Song J, Wang X, Liu J, Liu H, Li Y, Wang ZL. 2008. Piezoelectric potential output from ZnO nanowire functionalized with *p*-type oligomer. *Nano Lett.* 8:203–7

101. Su Y, Dagdeviren C, Li R. 2015. Measured output voltages of piezoelectric devices depend on the resistance of voltmeter. *Adv. Funct. Mater.* 25:5320–25
102. Su Y, Li S, Li R, Dagdeviren C. 2015. Splitting of neutral mechanical plane of conformal, multilayer piezoelectric mechanical energy harvester. *Appl. Phys. Lett.* 107:041905
103. Zheng Q, Shi B, Fan F, Wang X, Yan L, et al. 2014. In vivo powering of pacemaker by breathing-driven implanted triboelectric nanogenerator. *Adv. Mater.* 26:5851–56
104. Yang YL, Chuang MC, Lou SL, Wang J. 2010. Thick-film textile-based amperometric sensors and biosensors. *Analyst* 135:1230–34
105. Chuang MC, Windmiller JR, Santhosh P, Ramirez GV, Galik M, et al. 2010. Textile-based electrochemical sensing: effect of fabric substrate and detection of nitroaromatic explosives. *Electroanalysis* 22:2511–18
106. Leonov V, Leuven I, Torfs T, Fiorini P, Hoof CV. 2007. Thermoelectric converters of human warmth for self-powered wireless sensor nodes. *IEEE Sens. J.* 7:650–57
107. Pu X, Li L, Song H, Du C, Zhao Z, et al. 2015. A self-charging power unit by integration of a textile triboelectric nanogenerator and a flexible lithium-ion battery for wearable electronics. *Adv. Mater.* 27:2472–78
108. Yang W, Chen J, Zhu G, Yang J, Bai P, et al. 2013. Harvesting energy from the natural vibration of human walking. *ACS Nano* 7:11317–24
109. Zhou T, Zhang C, Han CB, Fan FR, Tang W, et al. 2014. Woven structured triboelectric nanogenerator for wearable devices. *ACS Appl. Mater. Interfaces* 6:14695–701

**TABLE OF CONTENTS FOR VOLUME 1:**

Annual Review of Biomedical Engineering
Volume 19, 2017

# Contents

**Indexes**



**Errata**

An online log of corrections to *Annual Review of Biomedical Engineering* articles may be found at http://www.annualreviews.org/errata/bioeng